n- and p-Type Doping Phenomenon by Artificial DNA and M-DNA on Two-Dimensional Transition Metal Dichalcogenides

Hyung-Youl Park,[†] Sreekantha Reddy Dugasani,[‡,§] Dong-Ho Kang,[†] Jeaho Jeon,[§] Sung Kyu Jang,[§] Sungjoo Lee,[†,§,∥] Yonghan Roh,[*,†,§] Sung Ha Park,[*,‡,§] and Jin-Hong Park[*,†]

[†]School of Electronics and Electrical Engineering, Sungkyunkwan University, Suwon 440-746, Korea, [‡]Department of Physics, Sungkyunkwan University, Suwon 440-746, Korea, [§]SKKU Advanced Institute of Nanotechnology (SAINT), Sungkyunkwan University, Suwon 440-746, Korea, and [∥]Center for Human Interface Nanotechnology (HINT), Suwon 440-746, Korea

ABSTRACT Deoxyribonucleic acid (DNA) and two-dimensional (2D) transition metal dichalcogenide (TMD) nanotechnology holds great potential for the development of extremely small devices with increasingly complex functionality. However, most current research related to DNA is limited to crystal growth and synthesis. In addition, since controllable doping methods like ion implantation can cause fatal crystal damage to 2D TMD materials, it is very hard to achieve a low-level doping concentration (nondegenerate regime) on TMD in the present state of technology. Here, we report a nondegenerate doping phenomenon for TMD materials (MoS_2 and WSe_2, which represent n- and p-channel materials, respectively) using DNA and slightly modified DNA by metal ions (Zn^{2+}, Ni^{2+}, Co^{2+}, and Cu^{2+}), named as M-DNA. This study is an example of interdisciplinary convergence research between DNA nanotechnology and TMD-based 2D device technology. The phosphate backbone (PO_4^-) in DNA attracts and holds hole carriers in the TMD region, n-doping the TMD films. Conversely, M-DNA nanostructures, which are functionalized by intercalating metal ions, have positive dipole moments and consequently reduce the electron carrier density of TMD materials, resulting in p-doping phenomenon. N-doping by DNA occurs at $\sim 6.4 \times 10^{10}$ cm^{-2} on MoS_2 and $\sim 7.3 \times 10^{9}$ cm^{-2} on WSe_2, which is uniform across the TMD area. p-Doping which is uniformly achieved by M-DNA occurs between 2.3×10^{10} and 5.5×10^{10} cm^{-2} on MoS_2 and between 2.4×10^{10} and 5.0×10^{10} cm^{-2} on WSe_2. These doping levels are in the nondegenerate regime, allowing for the proper design of performance parameters of TMD-based electronic and optoelectronic devices (V_{TH}, on-/off-currents, field-effect mobility, photoresponsivity, and detectivity). In addition, by controlling the metal ions used, the p-doping level of TMD materials, which also influences their performance parameters, can be controlled. This interdisciplinary convergence research will allow for the successful integration of future layered semiconductor devices requiring extremely small and very complicated structures.

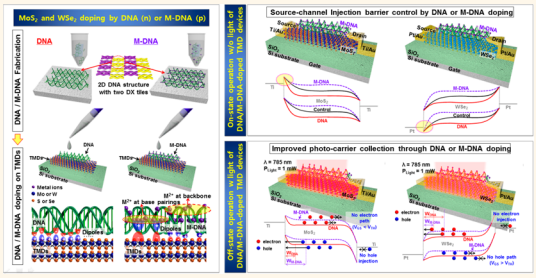

KEYWORDS: DNA · M-DNA · MoS_2 · WSe_2 · nondegenerate doping

Artificial deoxyribonucleic acid (DNA) nanostructures are currently being used in various nanoscale research fields including spintronics,[1,2] nanoelectronics,[3,4] biosensors,[5,6] and nanophotonics.[7,8] Due to the incredible flexibility of DNA base sequence design, diverse nanomaterials like proteins, nanoparticles (NPs), nanowires (NWs), and metal ions have been successfully attached to DNA nanostructures by simply modifying molecules in the DNA.[9−11] Yan *et al.* reported the successful self-assembly of discrete metal (Au and Ag) NP- and protein-based nanostructures on DNA templates.[9] The incorporation of metal ions (Cu^{2+}, Ni^{2+}, and Co^{2+}) into DNA base pairs was demonstrated by Shionoya *et al.*[12] and others,[13−15] subsequently creating functionalized DNA nanostructures. Additionally, the self-assembly of single-walled carbon nanotubes (SWNTs) into natural and origami templates of DNA was confirmed by Braun *et al.*[16] and Maune *et al.*[17] Although a field effect transistor (FET) device has been previously presented on the self-assembled SWNTs on DNA,[17] most research related to

* Address correspondence to yhroh@skku.edu, sunghapark@skku.edu, jhpark9@skku.edu.

Received for review August 29, 2014 and accepted October 27, 2014.

Published online October 29, 2014
10.1021/nn5048712

DNA-based nanostructures is stalled in the growth/synthesis stage and cannot yet be incorporated into the fabrication of electronic and optoelectronic devices.

Transition metal dichalcogenide (TMD) materials with two-dimensional (2D) layered structures are considered promising materials for next-generation wearable, flexible, stretchable, and transparent electronics due to their superior electrical, optical, and mechanical properties.[18−25] Their scalable thickness (down to the monolayer) and van der Waals epitaxial structure (ideally, no surface dangling bonds) free TMD-based thin film transistors (TFTs) from short channel effects (SCE) and carrier mobility degradation by surface oxidation/scattering.[18,26] In addition, changing the number of layers results in varied energy bandgaps, allowing for the development of various TMD-based 2D optoelectronic devices with wide spectral ranges from ultraviolet (UV) to near-infrared (IR).[23,24,26] However, since controllable doping methods like ion implantation can cause fatal crystal damage to 2D TMD materials, resent research has focused on developing a safe doping method that avoids crystal damage and allows for the successful integration of TMD-based 2D electronic and optoelectronic devices. Fang *et al.* reported a potassium-based degenerate n-doping process for molybdenum disulfide (MoS_2, typically serving as a n-channel TMD material in TFT) and tungsten diselenide (WSe_2, a p-channel TMD material in TFT) through surface charge transfer.[27] They used this method to form highly n-doped source/drain (S/D) regions in TMD-based 2D TFTs. Sreeprasad *et al.* also reported a method for n- and p-doping of MoS_2 through functionalization of Au NPs.[28] Moreover, n- and p-doping by polymers such as polyethylenimine (PEI) and functional self-assembled monolayers (SAMs) with different dipole moments were proposed by Du *et al.*[29] and Li *et al.*[30] Chen *et al.* reported p-doping of MoS_2 through selective area plasma treatment with fluorine (F) or oxygen (O).[31] Although these doping methods protected the crystallinity of TMD materials, they all are in a high-level doping concentration regime (degenerate), treating TMD materials as a near-metallic layer. In this light, a nondegenerate light doping technique (where TMD materials serve as semiconductors) that does not cause crystal damage is crucial for the design and fabrication of TMD-based 2D electronic and optoelectronic devices. However, nondegenerate doping on 2D TMD materials presents a major challenge because traditional ion implantation technique causes severe crystal damage. Recently, nondegenerate n- and p-doping of MoS_2 was achieved by Lin *et al.* using cesium carbonate (Cs_2CO_3) and molybdenum trioxide (MoO_3), respectively.[32,33]

Here, we also report nondegenerate n- and p-doping of TMD materials (MoS_2 and WSe_2, which are representative n- and p-channel materials, respectively) by both native DNA and M-DNA, slightly modified by metal ions (Zn^{2+}, Ni^{2+}, Co^{2+}, and Cu^{2+}). This research advances interdisciplinary convergence research between DNA nanotechnology and TMD-based 2D device technology. The phosphate backbone (PO_4^-) of DNA nanostructures attracts and holds hole carriers on the side of TMD, thereby n-doping the TMD films. Conversely, M-DNA nanostructures, which are functionalized by positive metal ions, have positive dipole moments and consequently are also predicted to have reduced electron carrier density in the TMD materials, resulting in p-doping. We investigated the doping of TMD materials by DNA or M-DNA in terms of the operations of electronic and optoelectronic devices using atomic force microscopy (AFM), Raman spectroscopy, and electrical/optical measurements (I_D-V_G with/without exposure to a 785 nm laser). By selecting different metal ions, we controlled the p-doping level of TMD materials and selectively influenced their performance parameters (V_{TH}, on-/off-currents, mobility, photoresponsivity, and detectivity).

RESULTS AND DISCUSSION

Synthesis and Analysis of 2D DNA and M-DNA Nanostructures on TMDs. In this experiment, we used a double crossover (DX) lattice structure with two repeating DX tiles (Supporting Information Figure S1 and Tables S1 and S2).[34] A single unit of the DX tile is organized such that two crossover junctions and two parallel duplexes are clinched up by the junctions. Panels a and b of Figure 1, show, respectively, AFM image schematics of DNA and M-DNA DX lattice fabrication by the free solution annealing method. Initially, we prepared a 1 M stock solution of all metal ions. Four different divalent metal ions (Zn^{2+}, Ni^{2+}, Co^{2+}, and Cu^{2+}) were added into the DX lattice at their optimal concentrations, in order to avoid structural deformation of the DX lattices.[35] The optimal concentration of each divalent metal ion was [Cu^{2+}] 4 mM; nickel ion [Ni^{2+}] 2 mM; zinc ion [Zn^{2+}] 1 mM; and cobalt ion [Co^{2+}] 1 mM. Initially, we conducted the experiment by adding metal ions into the DNA buffer solution before annealing in order to evaluate DNA crystal stability. Supporting Information Figure S2 shows the AFM images of Zn^{2+}−DNA with various [Zn^{2+}]. Here, deformation-free structures were observed up to 1 mM of [Zn^{2+}] and, beyond this concentration, we clearly confirmed the presence of deformation structures (Supporting Information Figure S2). A similar phenomenon was observed for other metal ions at different ion concentrations. To avoid structural deformation, we adopted the optimized metal ion doping concentration after the annealing procedure. To verify DX lattice formation, we performed AFM analysis again to visualize the DNA and Cu^{2+}−DNA DX lattices immobilized on a mica substrate. The insets in the top corners of Figure 1a,b are the noise-filtered 2D spectrum images after fast Fourier transform (FFT),

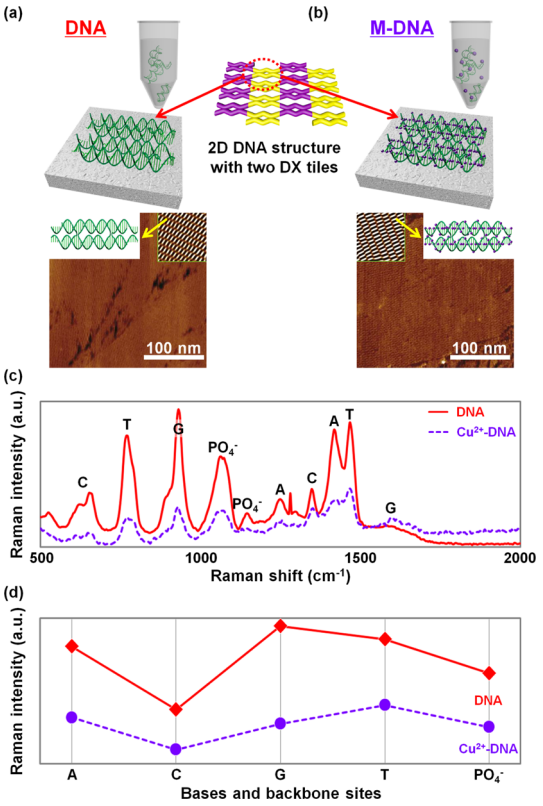

Figure 1. Schematic diagrams and AFM images of DNA and M-DNA DX lattice fabrication by free solution annealing method and the Raman spectra of DNA and M-DNA. (a and b) Schematic diagrams of DNA and M-DNA DX structure fabrication, and AFM images of pristine DNA and M-DNA with 4 mM Cu^{2+}. The insets in (a and b) are the noise-filtered 2D spectrum images with a scan size of 100 nm × 100 nm, showing the periodicity of the DNA and M-DNA lattices. (c) Raman spectra of DNA and Cu^{2+}–DNA. (d) The Raman intensity data as a function of bases and backbone sites (A, C, G, T, and PO_4^-). Here, we considered the strongest intensity of each A, C, G, T, and PO_4^-.

showing the clear periodicity of each DX lattice. The scale bars in all AFM images are 100 nm, and the inset size is 100 × 100 nm^2. The Raman spectra measured on DNA and M-DNA (Cu^{2+} 4 mM) structures are shown in Figure 1c. Raman signals were observed at 1246 and 1420 cm^{-1} for adenine (A); 770 and 1469 cm^{-1} for thymine (T); 931 and 1590 cm^{-1} for guanine (G); 618, 655, and 1348 cm^{-1} for cytosine (C); and 1066 and 1145 cm^{-1} for the phosphate backbone (PO_4^-) in DNA crystals without Cu^{2+}.[36,37] Figure 1d shows the extracted maximum intensity of A, C, G, T, and PO_4^- peaks in DNA and Cu^{2+}-DNA. The intensity of the bases and the backbone decreased after incorporating Cu^{2+} ions because the metal ions in the DNA molecules are preferably intercalated between the base-pairs and bound to the backbone sites. After correction for the reduced maximum intensity of each A, T, G, C, and PO_4^- Raman band was performed, their binding preferences were estimated to be 67–70% into base pairings (33–34% for A–T and 34–36% for G–C) and 30–33% into PO_4^- sites in backbones. Eichhorn *et al.* suggested that the metal ion binding sites in the DNA molecule were either phosphate groups or electron donor atoms on the heterocyclic bases.[38] Their report suggested that metal ions binding to phosphate sites stabilized the DNA helix, while metal ions intercalated between base-pairs destabilized the DNA helix. Lee *et al.*[15] also reported M-DNA with divalent metal ions intercalated between the base pairs. In that study, one to five Cu^{2+}-mediated base pairs of hydroxypyridone nucleobases were systematically incorporated into the middle of a DNA duplex in the solution phase.

After fabricating DNA and M-DNA nanostructures, the artificially designed DNA or M-DNA DX solution was dropped onto the MoS_2 and WSe_2 surfaces using a micropipette (40 μL) and dried three times, physically immobilizing the DX lattices onto the MoS_2 and WSe_2 surfaces. Here, the DNA nanostructures were homogeneously dispersed along the surface of MoS_2 and WSe_2. In the DNA-deposited TMD sample without metal ions, shown in Figure 2a, the phosphate backbone in DNA was expected to induce and hold positive charges (holes) at the interface region in the side of the TMD, resulting in n-doping. The M-DNA nanostructures with positive metal ions attracted negative charges (electrons) at the interface between DNA and TMD, resulting in p-type doping in the TMD films coated with M-DNA. Since we already confirmed two possible binding sites (A–T/G–C base pairings and PO_4^- in backbones) for metal ions through Raman spectroscopic analysis, as seen in Figure 2b, two cases of negative charge induction were predicted at the DNA–TMD interface. One was charge induction by the positive metal ions intercalated to DNA base pairs, and the other was induction by the metal ions at PO_4^- sites in DNA backbones. The metal ions bound at the base pairings and backbones seemed to similarly contribute to p-doping because their binding preferences were estimated to be 67–70% base pairings (33–34% for A–T and 34–36% for G–C) and 30–33% PO_4^- sites in backbones.

Raman Analysis of TMD Films Doped by DNA or M-DNA. To confirm that TMD can be doped by DNA or M-DNA through surface charge induction, Raman analysis with mapping was performed on TMD films coated by DNA or M-DNA. Figure 3 shows Raman spectra measured on MoS_2 and WSe_2 films doped by DNA and M-DNA (with metal ions of Zn^{2+}, Ni^{2+}, Co^{2+}, and Cu^{2+}). Two conventional peaks (E^1_{2g} and A_{1g}) were observed at ~380 and ~406 cm^{-1} in MoS_2 films, indicating the in-plane and out-of-plane vibrations for bulk TMD materials, respectively. In contrast, only a single peak at ~250 cm^{-1} was produced in WSe_2 films because both the E^1_{2g} and the A_{1g} modes for WSe_2 are close to 250 cm^{-1}.[39] The peak position shifts in E^1_{2g}, A_{1g}, and $E^1_{2g} + A_{1g}$ after DNA or M-DNA coating were extracted and plotted as shown in Figures 3b,d. In the DNA-coated TMD films, all of the peaks were red-shifted by

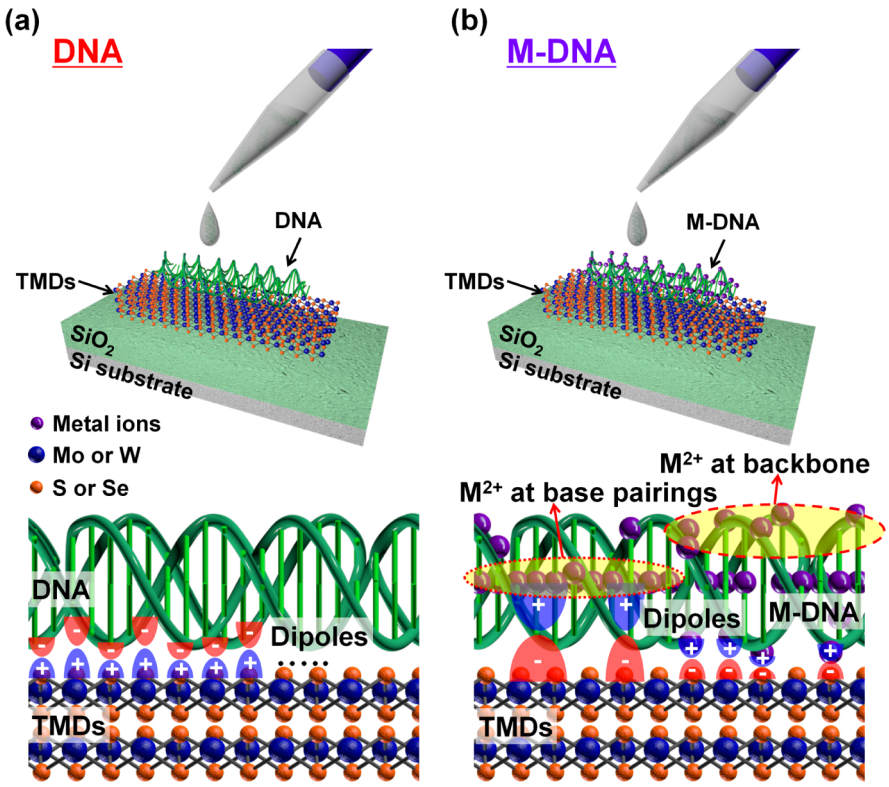

Figure 2. Doping mechanism of TMD films by DNA or M-DNA. (a) Schematic diagrams of DNA-deposited TMD sample showing n-type doping of TMD films by DNA. (b) Schematic diagrams of M-DNA-deposited TMD sample showing p-type doping of TMD films by M-DNA.

1.9−2.3 cm^{-1} (E^1_{2g}), 1.8−2.0 cm^{-1} (A_{1g}), or 1.8−2.2 cm^{-1} ($E^1_{2g} + A_{1g}$), indicating n-doping of both MoS_2 and WSe_2. This seemed to originate from positive charge induction at the DNA−TMD interface by the PO_4^- in DNA backbones. This red-shift was previously observed on MoS_2 and WSe_2 by several research groups studying functionalized Au nanoparticles,[28] polymers with different dipole moments.[30] In the M-DNA-coated TMD films, a blue-shift was observed in all peaks, indicating p-doping. When M-DNA nanostructures with Zn^{2+} and Ni^{2+} were used, the peaks were blue-shifted by 2.8−3.6 cm^{-1} (E^1_{2g}) and 3.7−3.8 cm^{-1} (A_{1g}) in the MoS_2 samples and 3.1−3.9 cm^{-1} ($E^1_{2g} + A_{1g}$) in WSe_2 samples. However, for the MoS_2 and WSe_2 films doped by M-DNA with Co^{2+} and Cu^{2+}, the peaks were pushed further to the right (ΔE^1_{2g} = ~5.0 cm^{-1}, ΔA_{1g} = ~5.2 cm^{-1}, and $\Delta E^1_{2g} + A_{1g}$ = ~5.1 cm^{-1}) compared with the peak shifts in Zn^{2+}− and Ni^{2+}−DNA samples. The positive charge strength of the nucleus seems to increase with corresponding increases in atomic number from 27 (Co) to 30 (Zn) due to the increasing atomic radius. However, when comparing Zn^{2+} and Co^{2+} at the same concentration (1 mM), M-DNA functionalized by Co^{2+} ions exhibits a much stronger p-doping phenomenon on MoS_2 and WSe_2. It is thought that Zn^{2+} ions with a larger radius are more difficult to attach in base pairings. In the case of Ni^{2+} and Cu^{2+} ions, the higher concentration (4 mM) of Cu^{2+} ions determined during the DNA crystal stability experiment is expected to lead to a stronger Cu^{2+}−DNA p-doping effect than Ni^{2+}−DNA on the TMDs. A similar blue-shift of the A_{1g} peak by 0.8−1.7 cm^{-1} was observed by Li *et al.* in MoS_2 flakes on substrates treated by octyltrichlorosilane (OTS) with a $-CH_3$ functional group and trichloro-(1*H*,1*H*,2*H*,2*H*-perfluorooctyl)silane (FOTS) with a $-CF_3$ functional group, with p-doping phenomenon confirmed through an electrical measurement.[30] Although the blue-shift in the Raman peak for WSe_2 has not previously been linked to doping, the blue-shift of the $E^1_{2g} + A_{1g}$ peak is also expected to be a result of p-doping because the change in the hole-phonon coupling of the A_{1g} mode is caused by p-doping of MoS_2.[30] We also predicted that the A_{1g} mode peak was a dominant component in the single peak since the E^1_{2g} mode is known to be weakly dependent upon doping.[30] As shown in Supporting Information Figure S3, the E^1_{2g}, A_{1g} and $E^1_{2g} + A_{1g}$ peaks in TMD films doped by only metal ions (no DNA templates) were blue-shifted by 1.8−3.8 , 2.4−3.8, and 1.8−3.8 cm^{-1}, respectively. Compared to M-DNA samples, the degree of blue-shift in the peaks was lower and had a larger error range. In doping by metal ions without DNA templates, it seems that fewer metal ions were nonuniformly and nonspecifically adsorbed on the TMD films because there were no negative charge sites for the metal ions. We also note

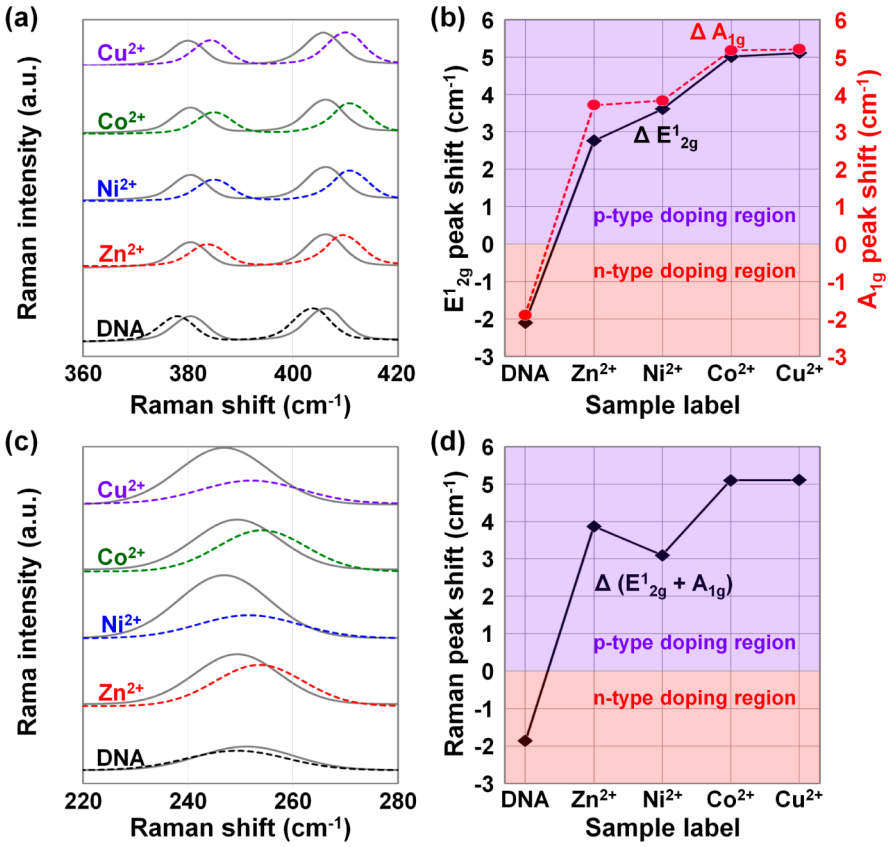

Figure 3. Raman analysis of TMD films doped by DNA or M-DNA. (a) Raman spectra of MoS_2 doped by DNA or M-DNA, and (b) extracted E^1_{2g} and A_{1g} peak shift data for MoS_2. (c) Raman spectra of WSe_2 doped by DNA or M-DNA, and (d) extracted $E^1_{2g} + A_{1g}$ peak shift data for WSe_2.

that ten samples were used for Raman analysis in each doping condition and Raman measurement was performed at five different points for each sample. Although 50 Raman peak position values were obtained for each doping condition, significant variation in peak position was not observed within each doping condition (Supporting Information Figure S4). Figure 4 shows Raman mapping images corresponding to E^1_{2g}, A_{1g}, and $E^1_{2g} + A_{1g}$ peaks in MoS_2 and WSe_2 before/after DNA and Cu^{2+}-DNA doping. Compared to undoped MoS_2 and WSe_2 flakes, darker and brighter MoS_2 and WSe_2 images were observed over the whole area after n- and p-doping, indicating that the MoS_2 and WSe_2 flakes were uniformly doped by the DNA and M-DNA. The color difference inside the flakes was most likely due to thickness variations because Raman peak position was dependent on the number of TMD layers.[39]

Electrical Characterization of DNA- or M-DNA-Doped TMD Electronic Devices. We fabricated and investigated MoS_2 and WSe_2 transistors doped by DNA or M-DNA (ten different devices for each doping condition) in order to reconfirm the n- and p-doping phenomena of TMDs. Figure 5a shows a schematic diagram of a MoS_2 transistor doped by M-DNA with the energy band diagrams of Ti-undoped/doped MoS_2–Ti junctions when a positive V_{DS} is applied. Compared to the control sample (undoped MoS_2), hole carriers are further accumulated at the interface between DNA and MoS_2 because DNA has a large number of PO_4^- sites with negative polarity, subsequently n-doping the MoS_2 region. Similarly in the case of M-DNA, positive metal ions attached at base pairings and backbones (PO_4^- sites) induce negative charges (electrons) at the M-DNA and MoS_2 interface, resulting in p-doping of MoS_2. n- and p-Doping of MoS_2 by DNA and M-DNA influence the tunneling probability of electron carriers from the source to MoS_2. In DNA-doped MoS_2, n-doping shifted the energy band to a lower value and increased the electric field at the source-MoS_2 junction. The raised electric field increased the tunneling probability of electrons and reduced the contact resistance, resulting in a negative shift in V_{TH}. In contrast, a positive V_{TH} shift occurred in the M-DNA-doped MoS_2 transistors. Figure 5b shows I_D–V_G characteristics measured at V_{DS} = 5 V, reflecting this positive V_{TH} shift (ΔV_{TH} = +4.6 V) after Cu^{2+}–DNA doping of the MoS_2 transistor. The on-current at V_{GS} = 20 V also decreased from 8 A/μm (control) to 1 A/μm after Cu^{2+}–DNA doping. As shown in Figure 5c, we then calculated the ΔV_{TH} (= V_{TH_DNA} (or $V_{TH\_M\text{-}DNA}$) − $V_{TH\_Control}$) and on-current ratio (=I_{on_DNA} (or $I_{on\_M\text{-}DNA}$) divided by $I_{on\_Control}$) of each sample. Negative (DNA-doping) and positive

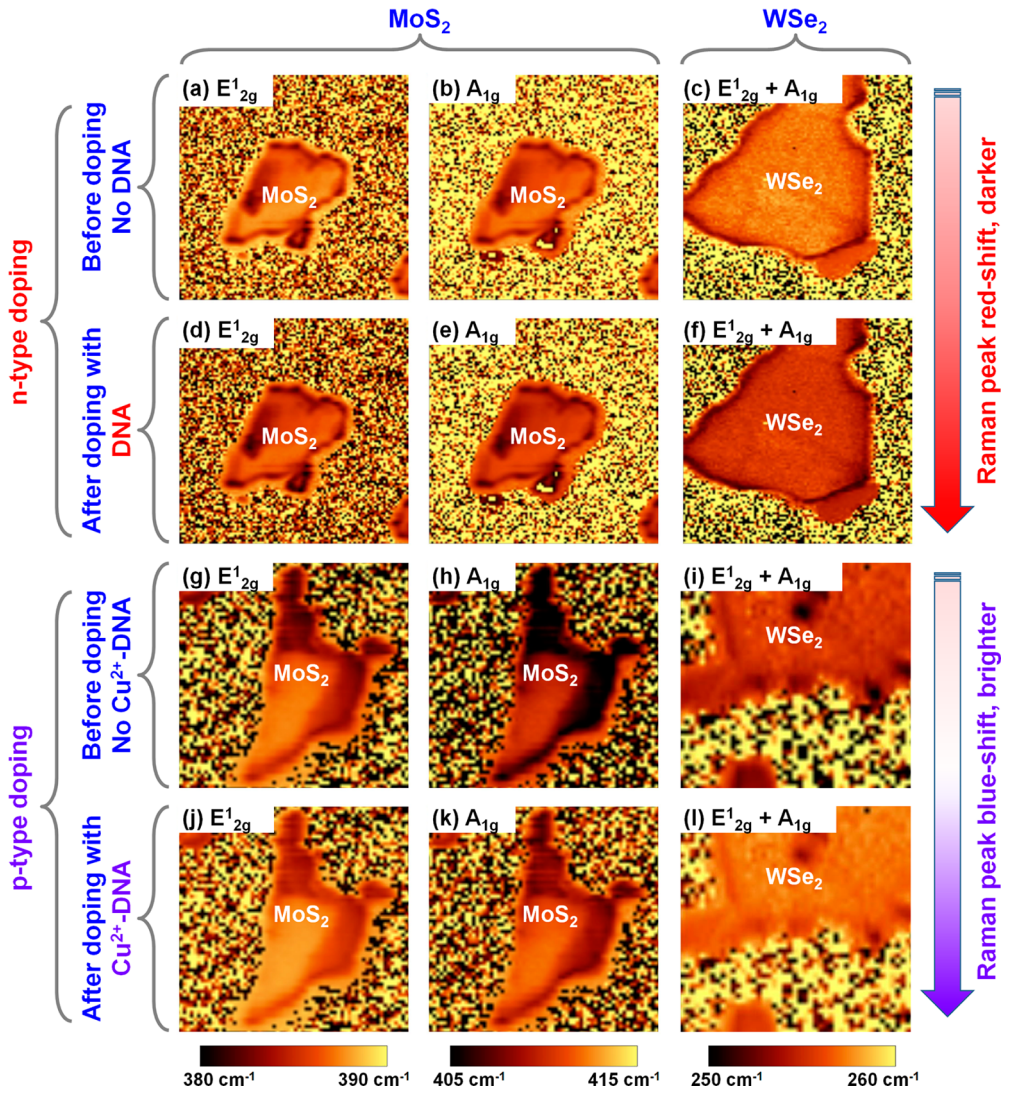

Figure 4. Raman mapping images of TMD films doped by DNA and Cu^{2+}–DNA. (a and d) E^1_{2g}, (b and e) A_{1g} peaks for MoS_2 and (c and f) $E^1_{2g} + A_{1g}$ peak for WSe_2 before (a, b and c) and after (d, e and f) n-doping by DNA. (g and j) E^1_{2g}, (h and k) A_{1g} peaks for MoS_2 and (i and l) $E^1_{2g} + A_{1g}$ peak for WSe_2 before (g, h and i) and after (j, k and l) p-doping by Cu^{2+}–DNA.

(M-DNA-doping) shifts in V_{TH} were observed in the MoS_2 transistors. A ΔV_{TH} of −3 V was obtained in the DNA-doped MoS_2 transistor and that of ∼1 V in the Zn^{2+}– and Ni^{2+}–DNA doped devices. For the transistors doped by Co^{2+} and Cu^{2+}–DNA, the V_{TH} was shifted further in the positive direction (ΔV_{TH} = 4.2−4.6 V) compared with the Zn^{2+}– and Ni^{2+}–DNA-doped devices, which is consistent with the blue-shift phenomenon in the E^1_{2g} and A_{1g} peaks described above. We also found a significant increase in on-current (on-current ratio = ∼7) after DNA n-doping, while the level of on-current was not significantly changed after M-DNA p-doping. We determined that a larger number of electron carriers may have accumulated in the channel region at the same $V_{GS} - V_{TH}$ due to the reduced effective electron barrier height after DNA-based n-doping. As shown in Figure 5d, we also extracted the field-effect mobility of the doped devices (at V_{DS} = 5 V and $V_{GS} = V_{TH}$) and found that the mobility (∼35 $cm^2\ V^{-1}\ s^{-1}$) of DNA-doped devices increased ∼8 times relative to the initial value (∼4 $cm^2\ V^{-1}\ s^{-1}$) of the control sample. However, in M-DNA-doped devices, an improvement in field-effect mobility was not observed because of the increased contact resistance in the source-MoS_2 junction. Here, the field-effect mobility values were roughly calculated from I_D–V_G characteristic curves without excluding a contact resistance effect for the next estimation of doping concentration. The 2D sheet doping concentration was calculated as n (or p) = $I_{DS}L/qW\mu V_{DS}$. The doping concentration after DNA n-doping increased from 3.8 × 10^{10} to 6.4 × 10^{10} cm^{-2} (Δn = ∼2.6 × 10^{10} cm^{-2}). Previously reported n-doping concentrations were ∼10^{13} cm^{-2} on MoS_2 doped by potassium, ∼5.6 × 10^{12} cm^{-2} by APTES, and ∼3.4 × 10^{12} cm^{-2} by FOTS.[30,40] In the M-DNA samples, negative Δn values of about −1.5 × 10^{10} cm^{-2} were obtained due to the reduction in electron carriers by the positive metal ions in M-DNA. Compared to

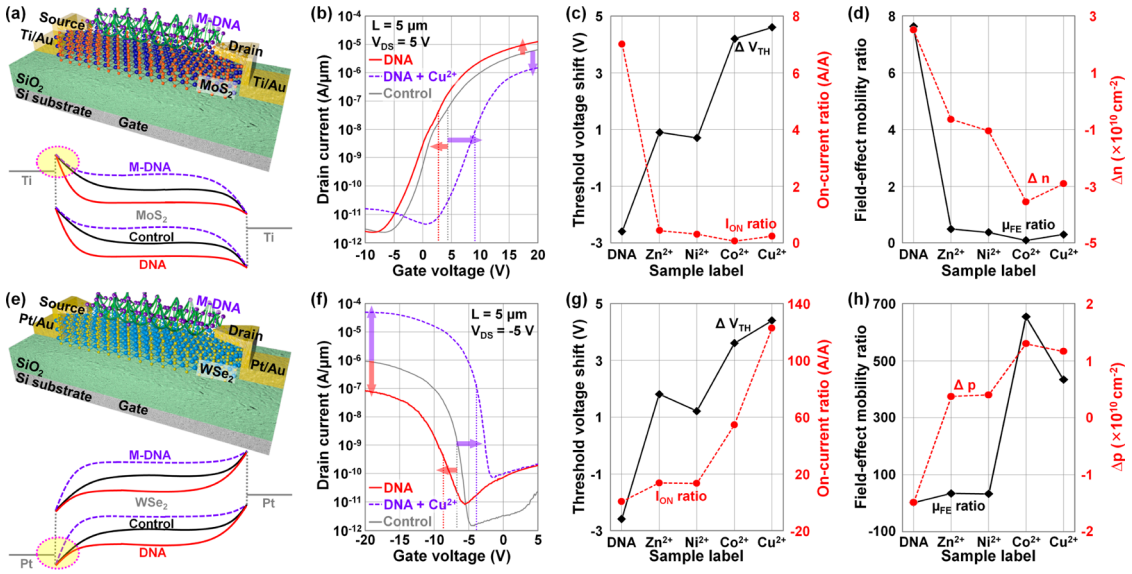

Figure 5. Schematic diagrams and electrical characterizations of TMD transistors doped by DNA and M-DNA. Schematic diagrams of back-gated transistor fabricated on (a) MoS_2 and (e) WSe_2 doped by M-DNA, along with the energy band diagrams of Ti-undoped/doped MoS_2–Ti and Pt-undoped/doped WSe_2–Pt junctions. I_D–V_G characteristics of the transistors fabricated on (b) MoS_2 and (f) WSe_2 films before/after DNA and Cu^{2+}–DNA doping. Threshold voltage shift (ΔV_{TH} = $V_{TH\_DNA\ or\ M\text{-}DNA} - V_{TH\_Control}$) and on-current ratio ($I_{on}$ ratio = $I_{on\_DNA\ or\ M\text{-}DNA}/I_{on\_Control}$) of (c) MoS_2 and (g) WSe_2 transistors before/after DNA and M-DNA doping. Field-effect mobility ratio (μ_{FE} ratio = $\mu_{FE\_DNA\ or\ M\text{-}DNA}/\mu_{FE\_Control}$) and variation of carrier concentration ($\Delta n = n_{\_DNA\ or\ M\text{-}DNA} - n_{\_Control}$, $\Delta p = p_{\_DNA\ or\ M\text{-}DNA} - p_{\_Control}$) in (d) MoS_2 and (h) WSe_2 transistors before/after DNA and M-DNA doping.

Zn^{2+}– and Ni^{2+}–DNA-doped devices, the further electron reduction in Co^{2+}– and Cu^{2+}–DNA samples was also consistent with the blue-shifted trend in the E^1_{2g} and A_{1g} peaks shown above.

Similar DNA and M-DNA doping was observed in WSe_2 films acting as p-channel materials due to the relatively low hole barrier height in the metal-WSe_2 junction. As shown in Figure 5e, n-doping by PO_4^- sites in the DNA backbone was expected to reduce the number of holes by increasing the effective hole barrier height in WSe_2 but not increasing the concentration of electron carriers, as it did in MoS_2. This was because the energy band of WSe_2 was down-shifted by DNA n-doping and eventually decreased the electric field in the left-side Pt-WSe_2 junction. However, in WSe_2 doped by M-DNA, the energy band was up-shifted, the tunneling probability of holes from the source to WSe_2 increased, and the concentration of hole carriers increased. Figure 5f shows the I_D–V_G characteristics of a WSe_2 transistor before/after Cu^{2+}–DNA doping, demonstrating a significant increase in on- and off-current levels from a reduction in the contact resistance of the Pt–WSe_2 junction. As seen in the case of MoS_2 transistors, higher positive shifts in V_{TH} (3.6–4.4 V) were observed in the WSe_2 transistors doped by Co^{2+}– and Cu^{2+}–DNA than those doped by Zn^{2+}– and Ni^{2+}–DNA (1.2–1.8 V). Since DNA with negative PO_4^- sites caused n-doping on WSe_2, a negative V_{TH} shift of about −2.6 V was obtained. Contrary to the MoS_2 transistors, an increase in on-current was observed in M-DNA samples because WSe_2 transistors had relatively lower hole barrier heights for hole injection, and the barrier height was further reduced by M-DNA p-doping. Small on-current enhancement (on-current ratio = ~13) was observed in the devices weakly doped by Zn^{2+}– and Ni^{2+}–DNA, but the on-current ratio dramatically increased to 58–125 when Co^{2+}- and Cu^{2+}-DNA were used to dope the WSe_2 films. In addition, the field-effect mobility slightly increased after doping with Zn^{2+}– and Ni^{2+}–DNA (31–43 $cm^2\ V^{-1}\ s^{-1}$), and mobility increased significantly in the devices strongly doped by Co^{2+}- and Cu^{2+}-DNA (430–650 $cm^2V^{-1}s^{-1}$). In devices n-doped by DNA, no increase in on-current or mobility was observed. According to the extracted 2D doping concentration data shown in Figure 5h, hole carrier concentration slightly increased from 2.2×10^{10} to 2.6×10^{10} cm^{-2} in Zn^{2+}– and Ni^{2+}–DNA samples (Δp = ~0.4×10^{10} cm^{-2}) and from 3.3×10^{10} to 4.8×10^{10} cm^{-2} (Δp = ~1.5×10^{10} cm^{-2}) in Co^{2+}– and Cu^{2+}–DNA samples. In devices n-doped by DNA, PO_4^- sites captured hole carriers in WSe_2, resulting in a Δp of about -1.5×10^{10} cm^{-2}. These electrical characterizations on the doped 2D TMD films reconfirmed doping of the 2D semiconductors (including TMDs) by DNA and M-DNA. We also elucidated how doping by DNA or M-DNA affects the performance parameters (V_{TH}, on-current, and field-effect mobility) of TMD-based electronic devices. Here, we also note that negligibly small variation was observed in ΔV_{TH} and on-current ratio even though ten different transistors were measured for each doping condition (Supporting Information Figure S5), and variation by solvent-doping (DI water, acetone, IPA,

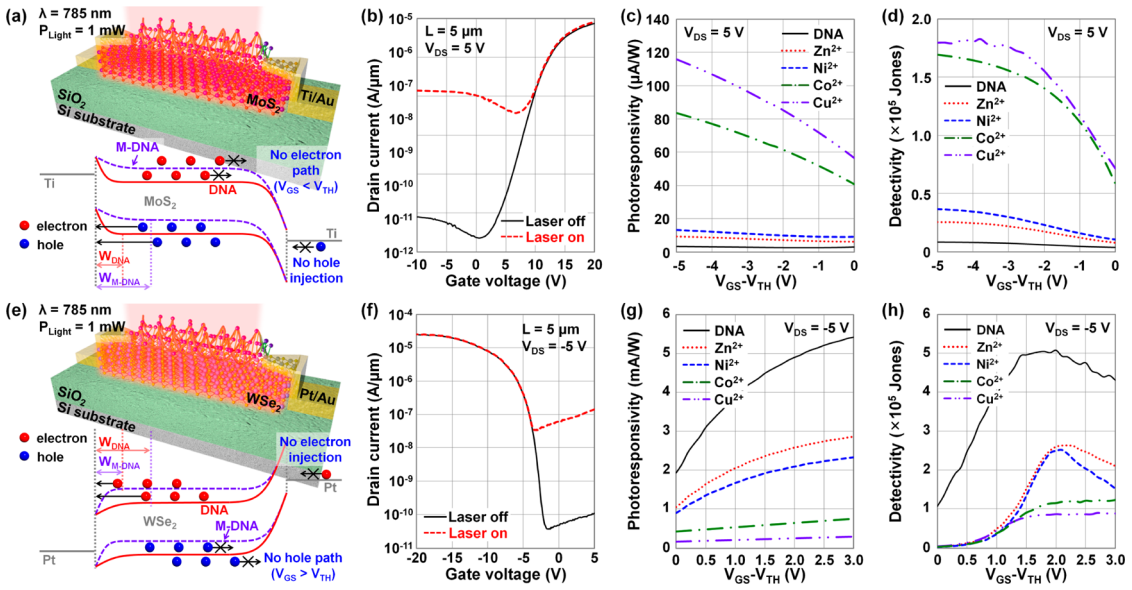

Figure 6. Schematic diagrams and characterization of TMD photodetectors doped by DNA and M-DNA. (a and e) Schematic diagrams showing the operation of DNA- or M-DNA-doped MoS_2/WSe_2 photodetectors with a light source (λ = 785 nm and P = 1 mW), and the energy band diagrams of Ti-MoS_2−Ti/Pt-WSe_2−Pt junctions under the illuminated condition. I_D−V_G characteristics of Cu^{2+}-DNA-doped (b) MoS_2 and (f) WSe_2 photodetectors before/after exposure to light. Photoresponsivity of (c) MoS_2 and (g) WSe_2 photodetectors as a function of V_{GS}−V_{TH} (in off-state). Detectivity of (d) MoS_2 and (h) WSe_2 photodetectors as a function of V_{GS}−V_{TH} (in off-state).

and 1 × TAE/Mg^{2+} buffer solution) in ΔV_{TH} and on-current ratio was also negligible. In particular, the ΔV_{TH} values of the doped MoS_2 and WSe_2 devices were not greatly changed even after 240 h of air-exposure (Supporting Information Figure S6). In the case of DNA-doped devices, ΔV_{TH} values were increased from −2.9 to −1.9 V in the MoS_2 device and from −2.8 to −1.8 V in the WSe_2 device, with a slight loss of the n-doping effect as a function of air-exposure time. In M-DNA-doped MoS_2 and WSe_2 devices, ΔV_{TH} values were decreased by 0.3−0.9 and 0.3−1 V, respectively, also indicating the weakening of the p-doping phenomenon after 240 h of air-exposure.

Characterization of DNA- or M-DNA-Doped TMD Optoelectronic Devices. Additionally, in order to investigate the effects of DNA or M-DNA doping on optoelectronic device performance, a photocurrent measurement was performed on the doped MoS_2 and WSe_2 photodetector devices, using a 785 nm laser source. Figure 6a shows a schematic diagram of the doped MoS_2 photodetector, along with the corresponding energy band diagrams of DNA and M-DNA-doped devices under negative V_{GS} ($V_{GS} < V_{TH}$, off-state) and positive V_{DS} bias condition. The photocurrent was only observed in the negative V_{GS} region (off-state) owing to the low dark current level under 10^{-5} A/μm, as seen in Figure 6b which presents I_D−V_G characteristics of Cu^{2+}−DNA-doped device before and after exposing the light. In the off-state, the absence of electron paths in MoS_2 (low electron current) and the high hole barrier height (low hole current) reduced the dark current level to the order of 10^{-6} A/μm. We then extracted and plotted photoresponsivity ($R = I_{Photo}/P_{Light}$) and detectivity ($D^* = (RA^{1/2})/(2eI_{Dark})^{1/2}$) values as a function of V_{GS}−V_{TH}, where the generated photocurrent (= $I_{Laser\_on} - I_{Laser\_off}$), P_{Light} is the total incident optical power, A is the effective area of the device, e is the absolute value of the electron charge (1.6×10^{-19} C), and I_{Dark} is dark current. Compared to the DNA-doped device, an increase in depletion width of the left-side MoS_2/Ti junction after M-DNA doping may help in collecting more photogenerated holes and consequently increasing photocurrent. In Figure 6c, M-DNA-doped devices show higher photoresponsivity values than DNA-doped samples due to higher photocurrents. The photoresponsivity measured in M-DNA devices strongly doped by Co^{2+}− and Cu^{2+}−DNA was much higher than those in Zn^{2+}- and Ni^{2+}-DNA-doped devices. As the V_{GS} increased to V_{TH}, the weakened conductivity of the hole channel reduced photoresponsivity. A similar trend was observed in detectivity (D^*), as shown in Figure 6d, and the highest value (maximum $D^* = \sim 1.79 \times 10^5$ Jones) was obtained in the Cu^{2+}−DNA-doped device. This was because detectivity can be expressed as the ratio of I_{Photo} to I_{Dark}, and the I_{Dark} is not dependent on variations in injection barrier height by different types of doping (n-type by DNA and p-type by M-DNA). Reductions in photocurrent and photoresponsivity resulting from V_{GS} increases decreased the detectivity values as a function of $V_{GS} - V_{TH}$.

In the WSe_2 device shown in Figure 6e, lower levels of photocurrent were expected after M-DNA-doping compared to DNA-doping because the narrowed

depletion region in the left-side junction results in a poor photocarrier collection. Figure 6f shows I_D-V_G characteristics before and after light exposure, measured on a Cu^{2+}–DNA-doped WSe_2 device, which confirmed a photocurrent in the off-state ($V_{GS} > V_{TH}$). Using the I_D-V_G curves of DNA- and M-DNA-doped devices, we also extracted and plotted photoresponsivity and detectivity as a function of $V_{GS}-V_{TH}$, as shown in Figure 6g,h. Much higher photoresponsivity (maximum: ~5.4 mA/W at $V_{GS} = V_{TH} + 3$ V) was observed in the DNA-doped device because its wider depletion region enhanced photocarrier collection (electrons). Among the M-DNA-doped devices, the strongly doped Co^{2+}– and Cu^{2+}–DNA samples presented the lowest photoresponsivity values (maximums were ~0.8 and ~0.4 mA/W at $V_{GS} = V_{TH} + 3$ V, respectively). In addition, the photoresponsivity slightly increased as V_{GS} positively rose because the left-side depletion widened through the down-shift of WSe_2 energy band. Due to increased photocurrent in the DNA-doped device, higher detectivity (maximum $D^* = \sim 4.3 \times 10^5$ Jones) was also observed, compared to that of M-DNA-doped samples. The Co^{2+}– and Cu^{2+}–DNA-doped devices showing strong p-type doping presented relatively low detectivity values around 10^5 Jones.

CONCLUSIONS

In summary, we reported nondegenerate doping phenomenon on TMD films (MoS_2 and WSe_2) using DNA and M-DNA with various metal ions (Zn^{2+}, Ni^{2+}, Co^{2+}, and Cu^{2+}). This work advances interdisciplinary convergence research between DNA nanotechnology and TMD-based 2D device technology. It is thought that the PO_4^- sites in DNA backbones hold hole carriers at the DNA–TMD interface region, thereby n-doping the TMD films. Conversely, since M-DNA nanostructures functionalized by conjugated metal ions have positive dipole moments, they reduce the electron carrier density in TMD materials and consequently induce p-doping on TMD films. The low levels of n-doping achieved by DNA on the MoS_2 and WSe_2 films (~6.4×10^{10} and ~7.4×10^9 cm^{-2}, respectively) were confirmed by Raman spectroscopy and I_D-V_G measurement. The p-doping concentrations by M-DNA were between 2.3×10^{10} and 5.5×10^{10} cm^{-2} on MoS_2 and between 2.4×10^{10} and 5.0×10^{10} cm^{-2} on WSe_2. In addition, Raman mapping images confirmed that the n- and p-doping were uniformly distributed across the TMD area. Both n- and p-doping levels were in the nondegenerate regime, allowing for the adjustment of the performance parameters of TMD-based electronic and optoelectronic devices (V_{TH}↑, on-/off-currents↑, field-effect mobility↑, photoresponsivity↓, and detectivity↓ by increasing doping concentration level). We also found a significant increase in on-current after DNA n-doping on the MoS_2 device and M-DNA p-doping on the WSe_2 device, because a larger number of carriers had accumulated in the channel region at the same voltage bias ($V_{GS} - V_{TH}$) due to the reduced effective barrier height after DNA and M-DNA doping. However, compared to the DNA-doped MoS_2 device (or the M-DNA-doped WSe_2 device), an increase in the depletion width of the left-side MoS_2/Ti junction after M-DNA doping (or the left-side WSe_2/Pt junction after DNA doping) helped in collecting more photogenerated holes (or electrons for the WSe_2 device) and, consequently, increasing photocurrent. By varying the type of metal ions attached to the DNA nanostructure, we controlled the p-doping level of TMD materials. Through this interdisciplinary convergence research between DNA nanotechnology and TMD-based 2D device technology, we hope to successfully integrate future layered semiconductor devices with extremely smaller and more complicated structures.

EXPERIMENTAL METHODS

DNA DX Lattice Fabrication. High-performance liquid chromatography (HPLC)-purified synthetic oligonucleotides of DNA were purchased from BIONEER (www.bioneer.com). Two DX tiles were used for the construction of a 2D DNA nanostructure that was fabricated by conventional free solution annealing process. Complexes were formed by mixing a stoichiometric quantity of each strand in physiological 1× TAE/Mg^{2+} buffer (40 mM Tris base, 20 mM acetic acid, 1 mM EDTA (pH 8.0), and 12.5 mM magnesium acetate) for DX structure. They were cooled slowly from 95 to 25 °C to facilitate hybridization by placing the microtubes in 2 L of boiled water in a Styrofoam box for at least 24 h. The final concentration of DX DNA lattices was 200 nM.

Metal Ion Coordination on DNA. After annealing DX lattices in a test tube, the appropriate amount of 1 M concentration of Cu^{2+} solution $[Cu(NO_3)]_2$ (4 mM), Ni^{2+} solution $[NiCl_2]$ (2 mM), Zn^{2+} solution $[ZnCl_2]$ (1 mM), or Co^{2+} solution $[CoCl_2]$ (1 mM) was added, and the mixture was incubated at room temperature for 24 h.

AFM Measurement on DNA and M-DNA. AFM measurement was performed in fluid tapping mode in 1 × TAE/Mg^{2+} buffer. A DNA-covered mica sheet was attached to the metal puck using instant glue and 5 μL of DX solution, then 30 μL of 1× TAE/Mg^{2+} buffer was dropped onto the mica, and 10 μL of 1× TAE/Mg^{2+} buffer was mounted onto the AFM tip [A NP-S oxide-sharpened silicon nitride tip (Veeco)]. AFM images were obtained by a Digital Instruments Nanoscope III (Veeco).

Characterizations of DNA- or M-DNA-Doped TMD Films. DNA or M-DNA/TMD/SiO_2/Si samples were investigated and compared with a control sample (TMD/SiO_2/Si) by PL/Raman spectroscopy (Alpha300 M+, WITec). Here, TMD bulk flakes with similar thickness (~32 nm for MoS_2 and ~26 nm for WSe_2) were selected in order to avoid the thickness effect. A Raman spectroscopy with an excitation wavelength of 532 nm was used, the laser beam size was approximately 0.7–0.9 μm, and the instrumental spectral resolution was less than 0.9 cm^{-1}. An integration time of 5 s and a spectrometer with 1800 grooves/mm were used.

Fabrication and Electrical Characterization of DNA- or M-DNA-Doped TMD Electronic Devices. For the fabrication of back-gated TMD

transistors, source/drain electrode regions were patterned (channel length and width are 5 μm) on TMD/SiO_2/Si samples by optical lithography, followed by 10 nm-thick Ti (for MoS_2) or Pt (for WSe_2) and 50 nm-thick Au deposition in an e-beam evaporator. Transistors were doped by DNA or M-DNA with different metal ions (Zn^{2+}, Ni^{2+}, Co^{2+}, and Cu^{2+}) and were electrically analyzed using an HP 4415B semiconductor parameter analyzer (I_D-V_D and I_D-V_G) and an HP 4284A precision LCR meter (C−V). The threshold voltage (V_{TH}), carrier concentration (n), and field-effect mobility (μ_{FE}) were calculated from I_D-V_G data. All drain currents (I_{DS}) were normalized according to the channel width (W). We used the equations $\mu_{FE} = L/(WV_{DS}C_{OX}) \times (\partial I_D/\partial V_{GS})$ and n (or p) $= I_{DS}L/qW\mu V_{DS}$, where q is the electron charge, L and W are the length and width of the channel, respectively, and the gate oxide capacitance per unit area (C_{OX}) is $\varepsilon_{OX} \times \varepsilon_0/t_{OX}$. For comparison with other doping studies performed with different numbers of layers of TMD films, we normalized the extracted 2D electron concentration values by the number of TMD layers.

Characterization of DNA- or M-DNA-Doped TMD Optoelectronic Devices. To investigate the optoelectronic properties of the fabricated DNA- or M-DNA-doped TMD devices, a current−voltage (I_D-V_G) measurement was performed under both dark and illuminated conditions. The light source was a dot laser with a wavelength of 785 nm and an optical power of 1 mW. For the characterization and comparison of the TMD optoelectronic devices doped by DNA or M-DNA with different metal ions (Zn^{2+}, Ni^{2+}, Co^{2+}, or Cu^{2+}), photoresponsivity (R) and detectivity (D^*) were calculated from I_D-V_G curves. R was I_{Photo}/P_{Light} and D^* was $(RA^{1/2})/(2eI_{Dark})^{1/2}$, where I_{Photo} is the generated photocurrent, P_{Light} is the total incident optical power, A is the effective area of the detector, e is the absolute value of electron charge (1.6×10^{-19} C), and I_{Dark} is the dark current.

Conflict of Interest: The authors declare no competing financial interest.

Acknowledgment. This work was supported by the Basic Science Research Program and Mid-career Researcher Program through the National Research Foundation of Korea (NRF) funded by the Ministry of Education, Science and Technology (Grant Numbers: 2011-0007997 and 2012R1A2A2A02046890), and the Human Resources Development program (No. 20124010203280) of the Korea Institute of Energy Technology Evaluation and Planning (KETEP) grant funded by the Korea government Ministry of Trade, Industry and Energy.

Supporting Information Available: Schematic diagram, sequence pool, and sticky-ends for the double crossover (DX) tiles. AFM images of DNA DX structures where various [Zn^{2+}] are incorporated. Raman spectrum analysis of TMD films doped by metal ions (no DNA). Raman and electrical analysis (ΔV_{TH} and on-current ratio) evaluating the reliability of the doping phenomenon in TMD films doped by DNA and M-DNA. Air-stability of DNA and M-DNA doping phenomena on MoS_2 and WSe_2 transistors. This material is available free of charge *via* the Internet at http://pubs.acs.org.

REFERENCES AND NOTES

1. Rikken, G. A New Twist on Spintronics. *Science* **2011**, *331*, 864–865.
2. Bader, S. D.; Parkin, S. S. P. Spintronics. *Cond. Mater. Phys.* **2010**, *1*, 71–88.
3. Braun, E.; Eichen, Y.; Sivan, U.; Ben-Yoseph, G. DNA-Templated Assembly and Electrode Attachment of a Conducting Silver Wire. *Nature* **1998**, *391*, 775–778.
4. Rakitin, A.; Aich, P.; Papadopoulos, C.; Kobzar, Y.; Vedeneev, A. S.; Lee, J. S.; Xu, J. M. Metallic Conduction through Engineered DNA: DNA Nanoelectronic Building Blocks. *Phys. Rev. Lett.* **2011**, *86*, 3670–3673.
5. Nam, J.-M.; Thaxton, C. S.; Mirkin, C. A. Nanoparticle-Based Bio-Bar Codes for the Ultrasensitive Detection of Proteins. *Science* **2003**, *301*, 1884–1886.
6. Lu, T.; Goldsmith, B. R.; Kybert, N. J.; Johnson, A. T. C. DNA-Decorated Graphene Chemical Sensors. *Appl. Phys. Lett.* **2010**, *97*, 083107.
7. Lewis, F. D. DNA Molecular Photonics. *Photochem. Photobiol.* **2005**, *81*, 65–72.
8. Seeman, N. C. DNA in a Material World. *Nature* **2003**, *421*, 427–431.
9. Yan, H.; Park, S. H.; Finkelstein, G.; Reif, J. H.; LaBean, T. H. DNA-Templated Self-Assembly of Protein Arrays and Highly Conductive Nanowires. *Science* **2003**, *301*, 1882–1884.
10. Sharma, J.; Chhabra, R.; Cheng, A.; Brownell, J.; Liu, Y.; Yan, H. Control of Self-Assembly of DNA Tubules through Integration of Gold Nanoparticles. *Science* **2009**, *323*, 112–116.
11. Pal, S.; Deng, S.; Ding, B.; Yan, H.; Liu, Y. DNA-Origami-Directed Self-Assembly of Discrete Silver-Nanoparticle Architectures. *Angew. Chem. Int. Edn. Engl.* **2010**, *49*, 2700–2704.
12. Tanaka, K.; Tegeiji, A.; Kato, T.; Toyama, T.; Shionoya, M. A Discrete Self-Assembled Metal Array in Artificial DNA. *Science* **2003**, *299*, 1212–1213.
13. Duguid, J.; Bloomfield, V. A.; Benevides, J.; Thomas, G. J. Raman Spectroscopy of DNA-Metal Complexes. 1. Interactions and Conformational Effects of the Divalent-Cation-Mg, Ca, Sr, Ba, Mn, Co, Ni, Cu, Pd and Cd. *Biophys. J.* **1993**, *65*, 1916–1928.
14. Switzer, C.; Sinha, S.; Kim, P. H.; Heuberger, B. D. A Purine-Like Ni^{2+} Base Pair for DNA. *Angew. Chem., Int. Ed.* **2005**, *44*, 1529–1532.
15. Lee, J. S.; Latimer, L. J. P.; Reid, R. S. A Cooperative Conformational Change in Duplex DNA Induced by Zn^{2+} and Other Divalent Metal Ions. *Biochem. Cell Biol.* **1993**, *71*, 162–168.
16. Keren, K.; Berman, R. S.; Buchstab, E.; Sivan, U.; Braun, E. DNA-Templated Carbon Nanotube Field-Effect Transistor. *Science* **2003**, *302*, 1380–1382.
17. Maune, H. T.; Han, S.-P.; Barish, R. D.; Bockrath, M.; Goddard, W. A.; Rothemund, P. W. K.; Winfree, E. Self-Assembly of Carbon Nanotubes into Two-Dimensional Geometries Using DNA Origami Templates. *Nat. Nanotechnol.* **2010**, *5*, 61–66.
18. Radisavljevic, B.; Radenovic, A.; Brivio, J.; Giacometti, V.; Kis, A. Single-Layer MoS_2 Transistors. *Nat. Nanotechnol.* **2011**, *6*, 147–150.
19. Kim, S.; Konar, A.; Hwang, W. S.; Lee, J. H.; Lee, J.; Yang, J.; Jung, C.; Kim, H.; Yoo, J. B.; Choi, J. Y.; *et al.* High-Mobility and Low-Power Thin-Film Transistors Based on Multilayer MoS_2 Crystals. *Nat. Commun.* **2012**, *3*, 1011.
20. Lembke, D.; Kis, A. Breakdown of High-Performance Monolayer MoS_2 Transistors. *ACS Nano* **2012**, *6*, 10070–10075.
21. Mak, K. F.; He, K.; Shan, J.; Heinz, T. F. Control of Valley Polarization in Monolayer MoS_2 by Optical Helicity. *Nat. Nanotechnol.* **2012**, *7*, 494–498.
22. Zeng, H.; Dai, J.; Yao, W.; Xiao, D.; Cui, X. Valley Polarization in MoS_2 Monolayers by Optical Pumping. *Nat. Nanotechnol.* **2012**, *7*, 490–493.
23. Lee, H. S.; Min, S. W.; Chang, Y. G.; Park, M. K.; Nam, T.; Kim, H.; Kim, J. H.; Ryu, S.; Im, S. MoS_2 Nanosheet Phototransistors with Thickness-Modulated Optical Energy Gap. *Nano Lett.* **2012**, *12*, 3695–3700.
24. Yin, Z.; Li, H.; Li, H.; Jiang, L.; Shi, Y.; Sun, Y.; Lu, G.; Zhang, Q.; Chen, X.; Zhang, H. Single-Layer MoS_2 Phototransistors. *ACS Nano* **2012**, *6*, 74–80.
25. Bertolazzi, S.; Brivio, J.; Kis, A. Stretching and Breaking of Ultrathin MoS_2. *ACS Nano* **2011**, *5*, 9703–9709.
26. Liu, W.; Kang, J.; Sarlar, D.; Khatami, Y.; Jena, D.; Banerjee, K. Role of Metal Contacts in Designing High-Performance Monolayer n-Type WSe_2 Field Effect Transistors. *Nano Lett.* **2013**, *13*, 1983–1990.
27. Fang, H.; Tosun, M.; Seol, G.; Chang, T. C.; Takei, K.; Guo, J.; Javey, A. Degenerate n-Doping of Few-Layer Transition Metal Dichalcogenides by Potassium. *Nano Lett.* **2013**, *13*, 1991–1995.
28. Sreeprasad, T. S.; Nguyen, P.; Kim, N.; Berry, V. Controlled, Defect-Guided, Metal-Nanoparticle Incorporation onto MoS_2 *via* Chemical and Microwave Routes: Electrical, Thermal, and Structural Properties. *Nano Lett.* **2013**, *13*, 4434–4441.

29. Du, Y.; Liu, H.; Neal, A. T.; Si, M.; Ye, P. D. Molecular Doping of Multilayer MoS_2 Field-Effect Transistors: Reduction in Sheet and Contact Resistances. *IEEE Electron Device Lett.* **2013**, *34*, 1328–1330.
30. Li, Y.; Xu, C.-Y.; Hu, P. A.; Zhen, L. Carrier Control of MoS_2 Nanoflakes by Functional Self-Assembled Monolayers. *ACS Nano* **2013**, *7*, 7795–7804.
31. Chen, M.; Nam, H.; Wi, S.; Ji, L.; Ren, X.; Bian, L.; Lu, S.; Liang, X. Stable Few-Layer MoS_2 Rectifying Diodes Formed by Plasma-Assisted Doping. *Appl. Phys. Lett.* **2013**, *103*, 142110.
32. Lin, J. D.; Han, C.; Wang, F.; Wang, R.; Xiang, D.; Qin, S.; Zhang, X.-A.; Wang, L.; Zhang, H.; Wee, A. T. S.; *et al.* Electron-Doping Enhanced Trion Formation in Monolayer Molybdenum Disulfide Functionalized with Cesium Carbonate. *ACS Nano* **2014**, *8*, 5323–5329.
33. Lin, D.; Zhong, J.; Li, H.; Zhang, H.; Chen, W. Modulating Electronic Transport Properties of MoS_2 Field Effect Transistor by Surface Overlayers. *Appl. Phys. Lett.* **2013**, *103*, 063109.
34. Winfree, E.; Furong, L.; Wenzler, L. A.; Seeman, N. C. Design and Self-Assembly of Two-Dimensional DNA Crystals. *Nature* **1998**, *394*, 539–544.
35. Dugasani, S. R.; Lee, N.; Lee, J.; Kim, B.; Hwang, S. U.; Lee, K. W.; Kang, W. N.; Park, S. H. Magnetic Characteristics of Copper Ion-Modified DNA Thin Films. *Sci. Rep.* **2013**, *3*, 1819.
36. Dugasani, S. R.; Kim, J. A.; Kim, B. H.; Rao, P. J.; Gnapareddy, B.; Vyas, C.; Kim, T. S.; Park, S. H.; Manchanda, V. A 2D DNA Lattice as an Ultra-Sensitive Detector for Beta Radiations. *ACS Appl. Mater. Interfaces* **2014**, *6*, 2974–2979.
37. Kulkarni, A.; Kim, B.; Dugasani, S. R.; Pranav, J.; Kim, J.; Vyas, C.; Vijay, M.; Kim, T. S.; Park, S. H. A Novel Nanometric DNA Thin Film as a Sensor for Alpha Radiation. *Sci. Rep.* **2013**, *3*, 2062.
38. Eichhorn, G. L. *Advances in Inorganic Biochemistry*. Elsevier: New York, 1982; Vol. 3, p 2.
39. Tonndorf, P.; Schmidt, R.; Bottger, P.; Zhang, X.; Borner, J.; Liebig, A.; Albrecht, M.; Kloc, C.; Gordan, O.; Zahn, D. R. T.; *et al.* Photoluminescence Emission and Raman Reponse of Monolayer MoS_2, $MoSe_2$, and WSe_2. *Opt. Express* **2013**, *21*, 4908–4916.
40. Najmaei, S.; Zou, X.; Er, D.; Li, J.; Jin, Z.; Gao, W.; Zhang, Q.; Park, S.; Ge, L.; Lei, S.; *et al.* Tailoring the Physical Properties of Molybdenum Disulfide Monolayer by Control of Interfacial Chemistry. *Nano Lett.* **2014**, *14*, 1354–1361.